DEVELOPMENT OF THREE-DIMENSIONAL TWO-PHASE FLOW MEASUREMENT SENSORS AND GAS-LIQUID TWO-PHASE FLOW DYNAMICS

Masahiro Furuya, Takahiro Arai, Taizo Kanai, Kenetsu Shirakawa

Central Research Institute of Electric Power Industry (CRIEPI)
2-11-1 Iwado-kita, Komae, Tokyo 201-8511, JAPAN

ABSTRACT

A two-phase flow often exhibits a complicated three-dimensional structure by nature even in a simple vertical pipe. In order to model such a complicated flow structure and to validate multiphase flow CFD, the authors have been developing sensors for a liquid film thickness and a two-phase flow mixture in a complex geometry. The devised liquid film thickness sensor can acquire multiple points (e.g. 16 × 32) on the sensor at a high sampling rate (5000 frames/s). One can bend the sensor to form a round pipe with a small diameter (e.g. 12 mm). We devise another sensor to acquire void fraction and phasic velocity distributions in a 10 × 10 rod-bundle geometry. The subchannel void sensor (SCVS) consists of 11-wire × 11-wire and 10-rod × 10 rod electrodes. The sensor acquires 521 points of void fraction in the same plane and phasic velocity at 1250 frames/s: 121 points in the subchannel center and 400 points near the rod surface. In order to quantify three dimensional velocity of each bubble, bubble paring scheme has been developed to analyze two sets of wir-mesh sensor data. The devised scheme was applied to the vertical upward air-water flow (jG=0.64m/s, jL=0.64m/s) in a large diameter pipe (i.d. 224mm). The bubble pairing scheme visualized the developing process of two-phase flow: large bubbles coalesced with each other to move toward the center, while the rest of bubbles broke up into smaller bubbles and decelerated.

1. INTRODUCTION

A bubble rising in a pool exhibits a complicated zigzag motion with its shape changing. It is difficult to predict even such a single bubble motion because of its complexity and sensitivity to the initial and boundary conditions. Direct numerical simulation (DNS) for multiple-bubbles motion requires enormous memory space and long calculation time due to the interactions among bubbles, and bubble breakup and coalescence.

Such bubble motions can be widely observed as a part of distillation and fermentation phenomena in food processing and petrochemical plants, and boiling heat transfer phenomena in fossil and nuclear power plants. Increasing bubble number density causes depletion of a surface liquid film. In the boiling and condensation heat transfer, the dry patch area and liquid film thickness on a surface determine the heat transfer coefficient.

Although these bubble motions and liquid film thickness are of industrial importance, it is yet difficult to visualize and acquire them quantitatively. A single-phase flow can be visualized at high temporal and spatial resolutions by acquiring a change of electric and/or magnetic field. On the contrary, visual observation of two-phase flow is almost impossible due to scattering and reflections of visible light on a liquid-vapor interface; e.g. observation behind a bubble. An electromagnetic wave with high wave number such as X-ray and γ-ray has high penetrability, though temporal and spatial resolutions are often low if the radiation dose rate is small [1].

The paper addresses the devised sensors for subchannel void and liquid film thickness distribution as well as three-dimensional phasic velocity estimation methods.

2. LIQUID FILM THICKNESS DISTRIBUTION SENSOR

2.1 Measurement Principle

Figure 1 shows photographs and illustration of the devised liquid film thickness distribution sensor [2]. The sensor is manufactured as a flexible printed circuit board, which consists of three conductive layers. The thickness is less than 0.2 mm so that one can bend to form a cylindrical shape. A measurement domain includes a pair of electrode: excitation and measurement electrodes. It is surrounded by a grounded electrode with a gap of insulation layer to suppress cross-talks among measurement domains. The grounded electrode is kept

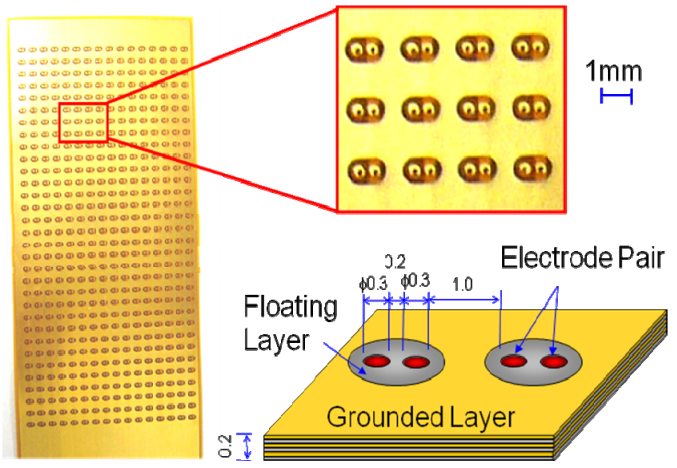

Unit: mm

Fig.1 Developed flexible thin sensor to acquire instantaneous liquid-film thickness distribution

at the rest potential, which is the electrochemical potential in the fluid (water). The sensor has 32 electrode pairs by 16 at intervals of 1.8 mm. All the electrodes were gold-plated for the corrosion resistance.

Figure 2 shows schematic of electric circuit and measurement procedures. Assuming that there are m electrode-pairs (row) by n electrode-pairs (line) to measure, required number of electrode cable is $m \times n \times 2$. Connecting each row and line respectively reduces the cable number down to $m + n$, which allows high surface density in a measurement domain. Only one row is excited at a time, and all the lines measure electric potential. The pulse is a bipolar rectangular signal to the rest potential. The measured electric potential estimates the film thickness on the measurement domain. The process repeats for the all rows to estimate the film thickness distribution over the sensor surface.

2.2 Electrochemistry and Equivalent Circuit

The sensor can estimate film thickness on the basis of electric potential of measurement electrode, which is affected by the excited electrode. The response of electric double layer determines the maximum measurement frequency. In order to quantify the dynamic response of electric double layer, the devised sensor was investigated by electrochemical impedance spectrometry.

Figure 3 shows a Bode diagram of the devised sensor. The amplitude and frequency of excited sinusoidal signal is 10 mV and ranges from 16 mHz to 100 kHz (at 10 points/decade). The blue solid line is gain, or amplitude. The gain at high frequency (>1 kHz) becomes approximately 10 kohms, which is liquid electric resistance. The gain at low frequency can be explained as a composition of liquid electric resistance and carrier mobility impedance. The red broken line is phase. The phase lag indicates capacitance of the electric double layer formed on the electrode.

Figure 4 shows a Nyquist diagram and the estimated equivalent electric circuit. The Nyquist diagram indicates that the circuit consists of capacitance and resistance of the electric double layer, and liquid resistance.

Figure 5 shows time series of signals of excited and measured signals. The excited pulse is a bipolar rectangular signal to the rest potential at 50 kHz. After each potential change, a spike signal was measured, and it decayed along the curves with the CR time constant. The response signals are identical for both cathodic and anodic polarization[3]. The frequency is equivalent to the 1000 frames/s for the devised sensor. The devised sensor can use up to the 1000 frames/s without significant interference of the electric double layer.

2.3 Application to Droplet Impingement on Liquid Film

As an example of liquid film transients, the devised sensor was applied to measure a liquid film thickness distribution by a droplet impingement. Figure 6 shows a series of photographs (upper) and acquired liquid film thickness distribution (lower). The initial film thickness and droplet diameter were approximately 1 mm and 4 mm, respectively. The surface plot of acquired film thickness clearly demonstrates the droplet impingement process at high spatial and temporal resolutions.

2.4 Application to Liquid Film Flow on Rod Surface

The devised sensor is thin (< 0.2 mm) and flexible to form a cylindrical surface. Figure 7 (on the left) shows a cylindrical

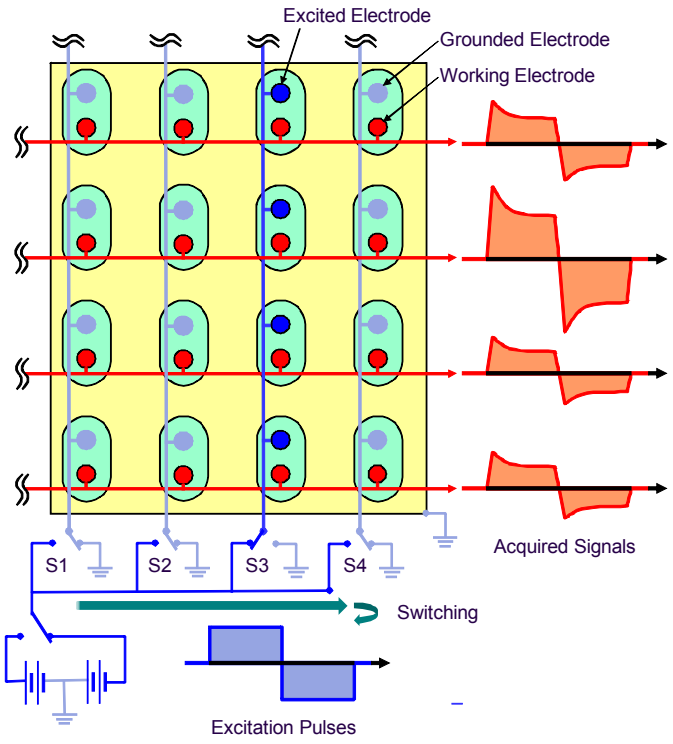

Fig.2 Measurement principle and signal processing procedure

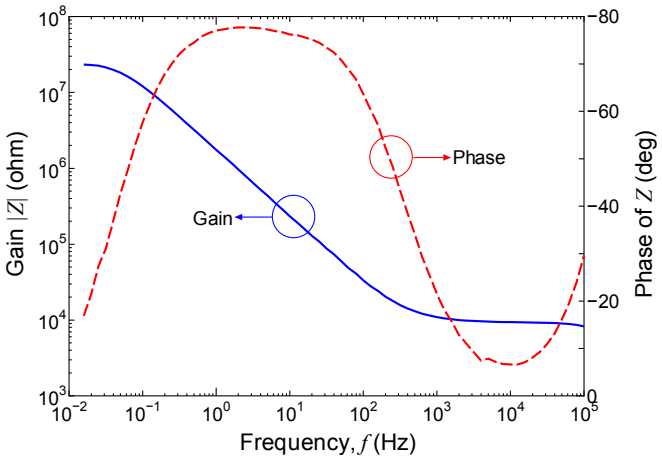

Fig.3 Bode diagram

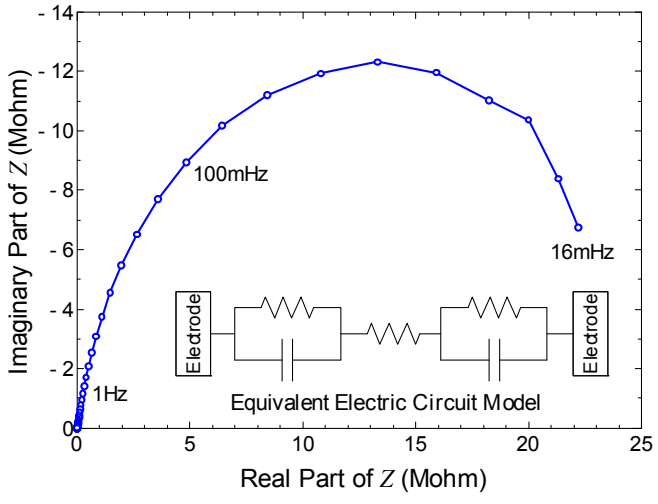

Fig.4 Nyquist diagram

sensor with diameter of 12 mm. All the measurement cables pass through inside of the cylinder not to intervene the flow. The sensor was inserted in a pipe (i.d. 18 mm). Water is injected at $j_L = 0.03$ m/s through a sintered metal nozzle into an air flow at $j_G = 20$ m/s in the annular channel to form a liquid film flow. As illustrated in the figure 7, the cubic flow obstacle (5 mm^W × 1 mm^H × 100 mm^L) was placed on the surface 200 mm downstream from the sintered metal nozzle. The figure 7 (on the right) shows the circumferential film thickness distribution at 5 mm downstream of the flow obstacle as a function of elapsed time. The darker blue color means the thicker film thickness. The periodical structures with 70 ms can be seen without the flow obstacle. On the other hand, fine flow structures can be seen with the flow obstacle due to the mixing effect of the flow obstacle. The sensor acquires film thickness distributions for 32 points by 16 points at 1000 frames/s for such high-velocity film-flow.

3. THREE-DIMENSIONAL BUBBLY FLOW MEASUREMENT SENSOR

3.1 Measurement Principle

Figure 8 illustrates a WMS structure to measure the void fraction distribution in a pipe. H. M. Prasser and his coworkers [3] have developed WMS and the methods to measure the void fraction distribution and one dimensional velocity. When only one wire is excited, void fraction can be attained by measuring an electric potential of another wire which is perpendicular to the excited wire [4]. All the other wires are kept at the rest potential to suppress crosstalk among wires.

In this study, the WMS consists of 64 excitation wires by 64 measurement wires with a pitch of 3.5 mm. The diameter of wires is 0.25 mm. The excitation and measurement wire layers are separated by 2.8 mm. Two sets of WMS can estimate phasic velocity on the basis of a time lag from one WMS to another.

The advantage of WMS is to capture two-phase flow structure at high temporal and spatial resolutions. The disadvantage of WMS is intrusive method. The sensor wires disturb a flow structure when the liquid superficial velocity is lower than 0.5 m/s [5]. One must recall these pros and cons to investigate three-dimensional two-phase flow dynamics.

3.2 Three-Dimensional Velocity Vector Estimation

The time-series data acquired with WMS are three dimensional void fraction data, $\alpha(x, y, t)$. The authors suggest evaluating each bubble property. The volume force of a relatively large bubble affects momentum of the bubble motion significantly. On the contrary, a relatively smaller bubble (< 1 mm) inherently accommodate to the surrounding fluid due to the interfacial friction force. The individual bubble identification is useful to evaluate bubbly flow dynamics.

In this study, each bubble is identified on first WMS ($i = 1$) and second ($i = 2$) from the void fraction data $\alpha_i(x, y, t)$. The position and volume of each bubble on each WMS plane is calculated as $p_i(x, y, t)$ and $V_i(x, y, t)$. The bubble pairing algorism picks up one bubble on the first WMS to seek another bubble on the second WMS, which has a close volume to each other. The pairing criteria are the two conditions: the time lag is less than 8 ms and the distance is less than 40 mm apart on the WMS plane. The paring criteria must be optimized in balance of missing and mispairing. Finally, each bubble velocity can be determined by the paired bubbles $u_i(x, y, t)$.

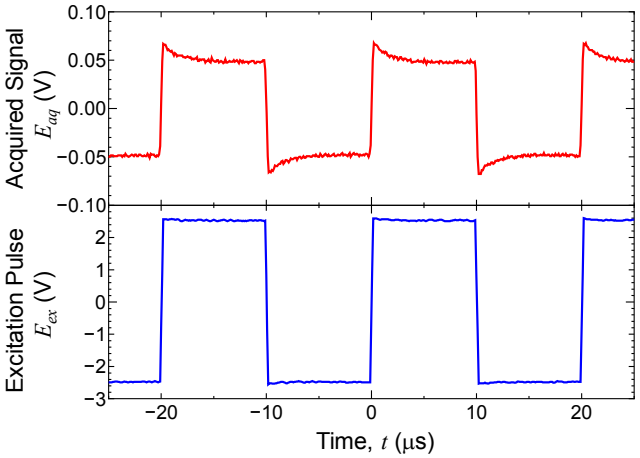

Fig.5 Time trace of excitation pulses and acquired signals

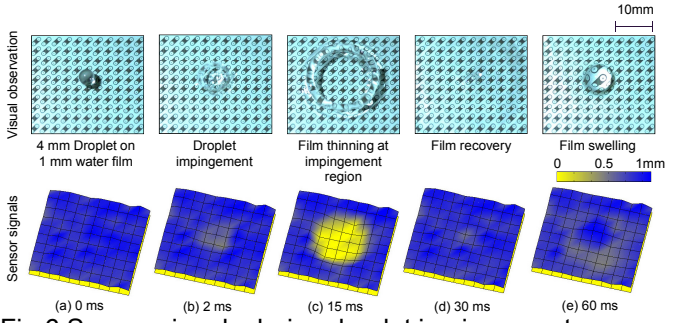

Fig.6 Sensor signals during droplet impingement process

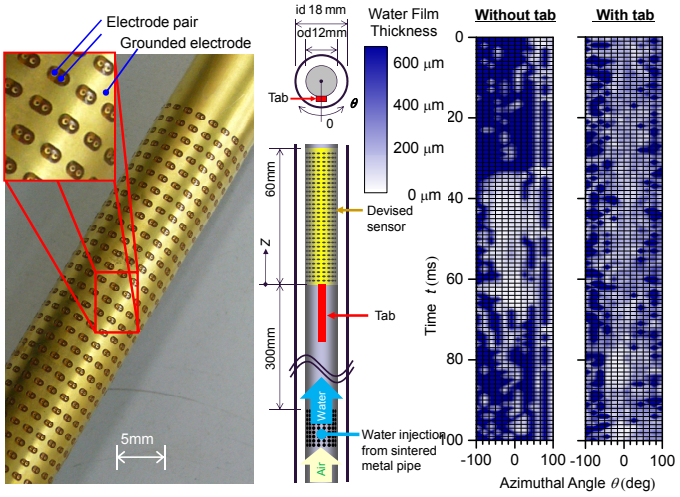

Fig.7 Sensor signals of water film flow on after tab (flow obstacle) in annulus: $Z = 5$ mm, $j_L = 0.03$ m/s, $j_G = 20$ m/s

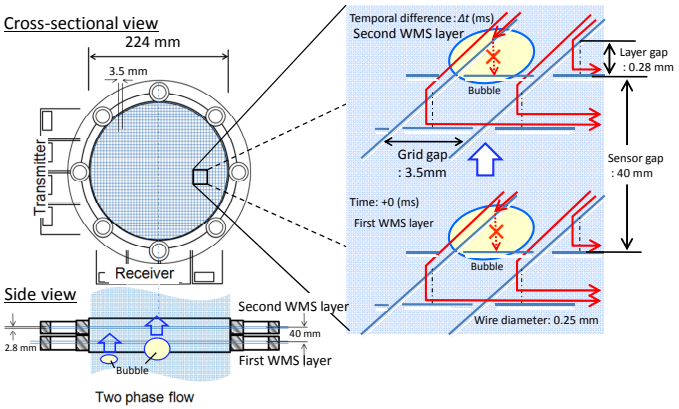

Fig.8 Measurement principle of WMS : Two sets of WMS to evaluate phasic velocity

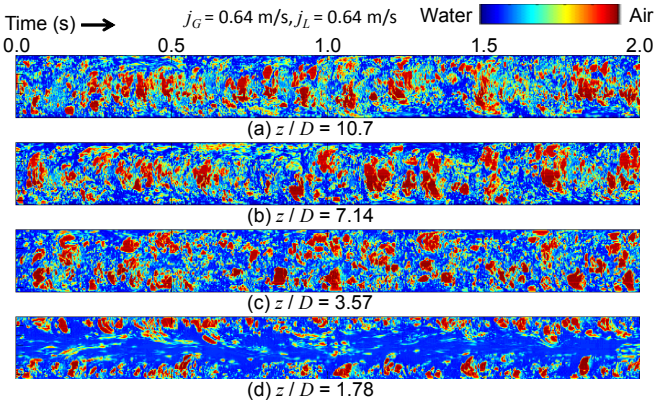

Fig.9 Cross-sectional Void Fraction Distribution

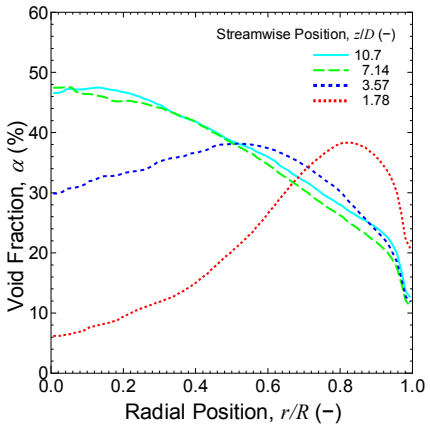

Fig.10 Radial Distribution of Void Fraction

3.3 Application to Bubbly Flow in Large Diameter Pipe

The bubble pairing algorism is successfully applied in the vertical polyvinyl-chloride pipe (i.d. 224 mm). Air was injected by 16 nozzles (i.d. 10 mm, 30 degrees apart) from the pipe surface into a fully-developed water flow at 30 °C. The lower end of the pipe is subjected to the ambient air (atmospheric pressure). The nondimensional distances of WMS from the nozzle, z/D are 1.78, 3.57, 7.14, and 10.7. Superficial gas velocity is j_G = 0.64m/s. Sampling rate and duration of WMS is 1000 frames/s and 5 s.

Figure 9 shows cross-sectional void fraction distributions in $\alpha(x, t)$. Figure 10 shows radial distribution of void fraction. As shown in the figures 9 (d), and 10 for z/D = 1.78, most of the bubble appears near the wall (r/R = 1) where air is injected. As the flow develops, the peak of the void fraction shifts to the center of the pipe.

Figure 11 shows the velocity vector of each bubble on the first WMS plane. Only 1000 bubbles from the largest are plotted to avoid messy plot. The bubble size is classified into

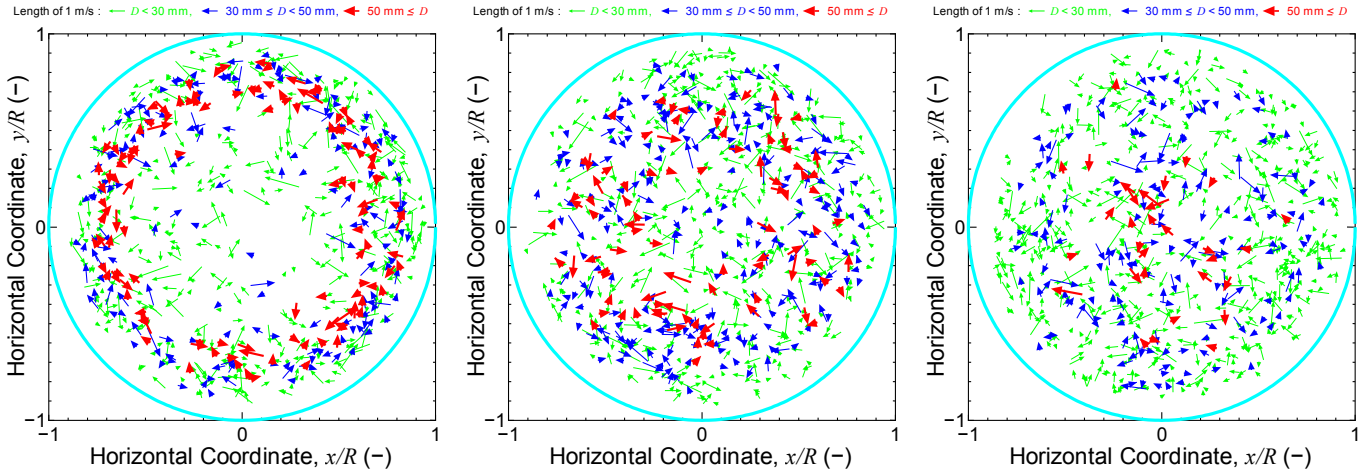

(a) z/D = 1.78 (b) z/D = 3.57 (c) z/D = 10.7

Fig.11 Velocity vector of each bubble on horizontal cross-section

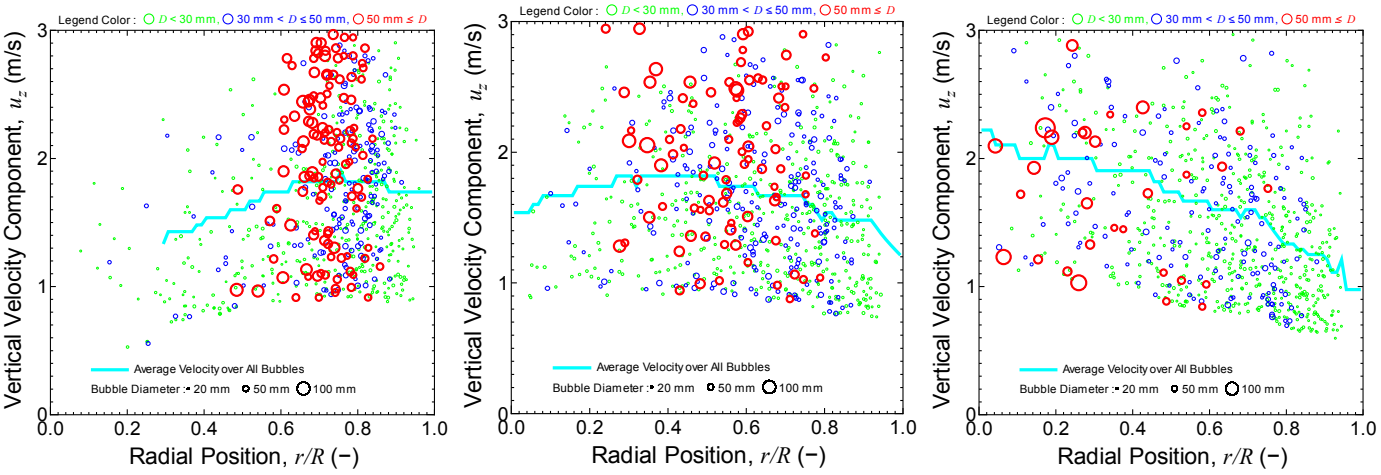

(a) z/D = 1.78 (b) z/D = 3.57 (c) z/D = 10.7

Fig.12 Bubble plot and radial profile of vertical velocity component of each bubble

three and plotted as three different arrow colors. At z/D = 1.78 in the figure 11 (a), most bubbles are stay near the wall. At z/D = 3.57 in the figure 11 (b), the larger bubbles moves to the center. At z/D = 10.7 in the figure 11 (c), the larger bubbles crowded in the center. In addition, the arrow size is laeger for the smaller bubble, since the smaller bubbles tend to move in the center after the larger bubbles at high velocity.

Figure 12 is a bubble plot and radial profile of the vertical component of each bubble. The solid curve in the figure is estimated on the basis of time lag of the first WMS raw signal to the second [5] without using the bubble pairing algorism. The circle symbol size is proportional to the diameter of the bubble. There are three circle symbols indicating in the figure for size example. Only 1000 bubbles from the largest are plotted to avoid messy plot. At z/D = 1.78 in the figure 12 (a) most of the bubbles are found near the pipe wall. At z/D = 3.57, bubbles moves toward the center and coalesces with each other. At z/D = 10.7, some bubbles grows in size and stays in the center, while the rest of the larger bubbles breakup into the smaller bubbles. This is because of the share force created by the larger bubbles. The vertical velocity is low near the wall, since there are smaller bubbles only where the phasic velocity is close to the liquid velocity due to the interfacial drag force. Three dimensional velocities estimated bubble pairing algorism gives detailed flow structure and suitable for modeling of bubble dynamics.

4. SUBCHANNEL VOID SENSOR (SCVS)

The previous section devotes to the measurement method in a large diameter pipe. This section address void signals in the rod (or tube) bundle geometry. It can be seen in nuclear reactor cores, steam generators, and heat exchangers, and so on. Such complex internal structures allow a straight wire to insert only through the rod gaps. The following section devotes to the devised sensor for high spatial resolution.

4.1 Measurement Principle

Figure 13 is a schematic of a SubChannel Void Sensor (SCVS). The design of SCVS is based on the 10×10 rod bundle geometry in a BWR core. The outer diameter of the rod is 10 mm, and rod pitch is 13 mm. 11-wires by 11-wires were inserted in the gaps between the rods, and acts as electrodes. 11 wires of both layers cross at 90 degrees with a gap of 2 mm. The diameter of the wires is 0.2 mm. The electric potential at the cross point of one wire to another measures the local void fraction in the center subchannel region at 121 points (= 11×11).

A unique feature of the devised sensor is use of rods as electrodes to measure the void fraction near rod surface. One rod is surrounded by four wires. In total, rod surface measurement locations are 400 points (= 10×10×4). Therefore, the sensor was able to measure overall 512 points of the local void fraction (= 121 + 400). In the same manner as WMS, SCVS is consists of an excitation electrode and measurement electrode. Figure 14 shows a cut away schematic of the electric circuit. When switch S1 is closed, an excitation pulse is supplied to the rod electrode E1. The pulse is a bipolar rectangular signal to the rest potential, which is the electrochemical potential in the fluid (water). An electric potential is acquired by each surrounding measurement electrode, and then estimates a void fraction near the rod surface. The process of switch S1 repeats to the switch S2, S3, S4, and so on.

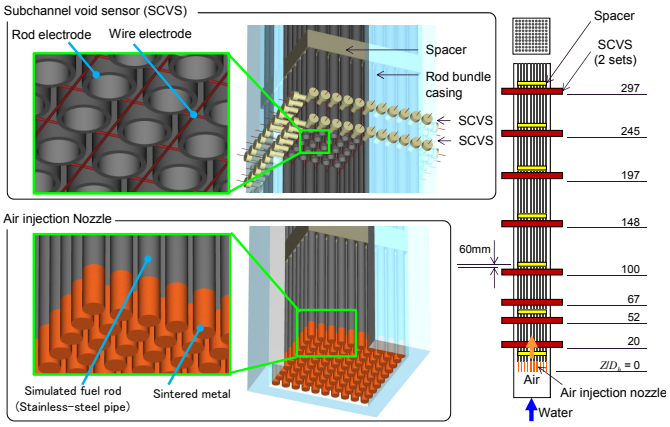

Fig.13 Schematic of devised subchannel void sensor (SCVS) to acquire two-phase flow dynamics in bundle geometry

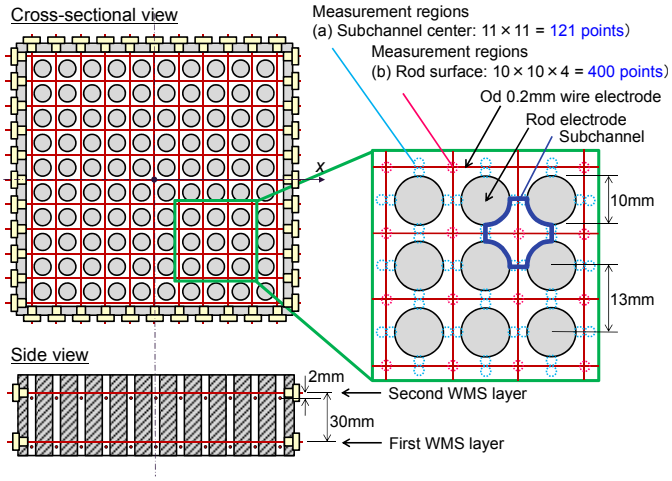

Fig.14 Assembly and 521 measurement points of SCVS, subchannel center: 121 points, rod surface 400 points

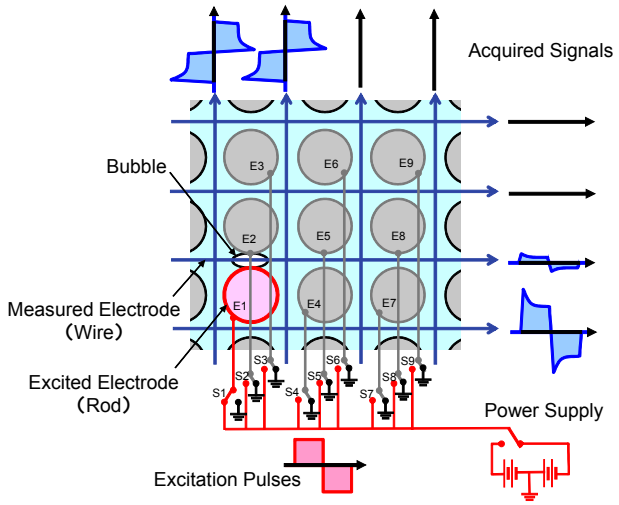

Fig.15 Measurement principle and signal processing procedure of rod excitation and wire measurement electrodes

4.2 Application to 10x10 Rod Bundle

Figure 15 is a schematic of the square channel with 10×10 rod bundle with SCVS. Air bubbles were injected in a vertical-upward water flow at the bottom end of the rods through sintered metal nozzles. The axial length scale, z, is a distance from the air nozzle. Hydraulic diameter, D_h, is 10.6 mm. Figure 16 is air-water two-phase flow for $j_L = 0.50$ m/s and $j_G = 0.61$ m/s. The figures show void fraction distribution, phasic velocity distribution, and histogram of chord length. The data were acquired at three different height levels: Z/D_h = 52, 100 and 293. The color scale on the top is common for three height levels. The histogram of chord length is normalized by time-average for two regions: center 4×4 bundle regions and rest of the bundle regions.

Figure 16 (c) is obtained at Z/D_h = 52, near the air nozzle. Since the air is injected at the peripheral air-nozzle only, the maxima in the void fraction and phasic velocity are in the peripheral part of the bundle. The peak value of chord length is 10 mm. As the flow develops toward downstream, the maxima in the void fraction and phasic velocity shift to the center. The peak value of chord length becomes 3 mm at Z/D_h = 100. The breakup of the bubbles is caused by the shear force due to the rapid profile change in the void fraction and phasic velocity. On the other hand, the longer chord length can be found at center and Z/D_h = 293. The bubbles moves to the center and coalesced to increase the size.

Figure 17 is a comparison of SCVS results to the results of four-sensor conductive prove by Paranjape *et al.*[6]. Paranjape *et al*. classified bubbles in two groups whether bubble diameter is smaller (group 1) or larger (group 2) than 5 mm. The void fraction distribution in the figure 17 (a) and phasic velocity distribution in the figure 17 (b) indicated that these values near the rod surface is larger than these at the center for both measurement systems.

SCVS can acquire three-dimensional profiles simultaneously, while a point prove sensor needs traverse system to acquire different points. The authors are going to measure the boiling two-phase flow at BWR conditions (7.2 MPa and 288 °C) with SCVS.

5. CONCLUDING REMARKS

In order to acquire three dimensional two-phase flow structures at CFD quality, the following sensors and measurement methods are devised and demonstrated.

(1) Liquid film thickness distribution sensor : the sensor can acquire multiple points on the surface (flat or rod surface) at a high sampling rate (5000 frames/s).
(2) Three-dimensional bubbly flow measurement sensor : the senor can estimate each bubble characteristics including position, volume, chord length and three dimensional velocity vector.
(3) Subchannel void sensor (SCVS) : SCVS can measure void fraction, chord length and phasic velocity at the subchannel center and rod surface in a rod bundle channel.

ACKNOWLEDGEMENTS

The authors like to send their greatest gratitude to Professor H.-M. Prasser of ETH, Zurich for his variable discussions on the sensor development. They are grateful to Takeo Yoshioka of CERES, and Yoshiyuki Shiratori, Hirokazu Kamata and

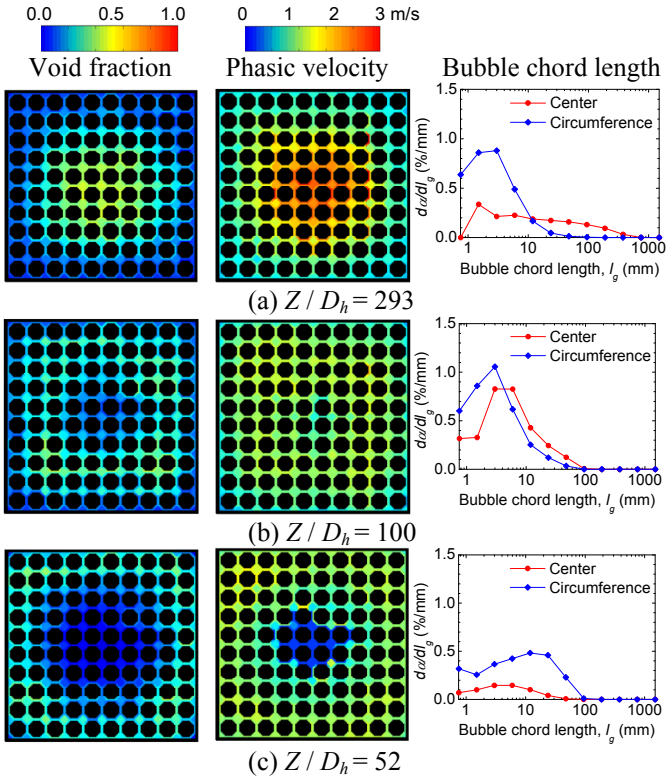

Fig.16 Air-water two-phase flow in 10×10 bundle geometry $j_L = 0.50$ m/s, $j_G = 0.61$ m/s

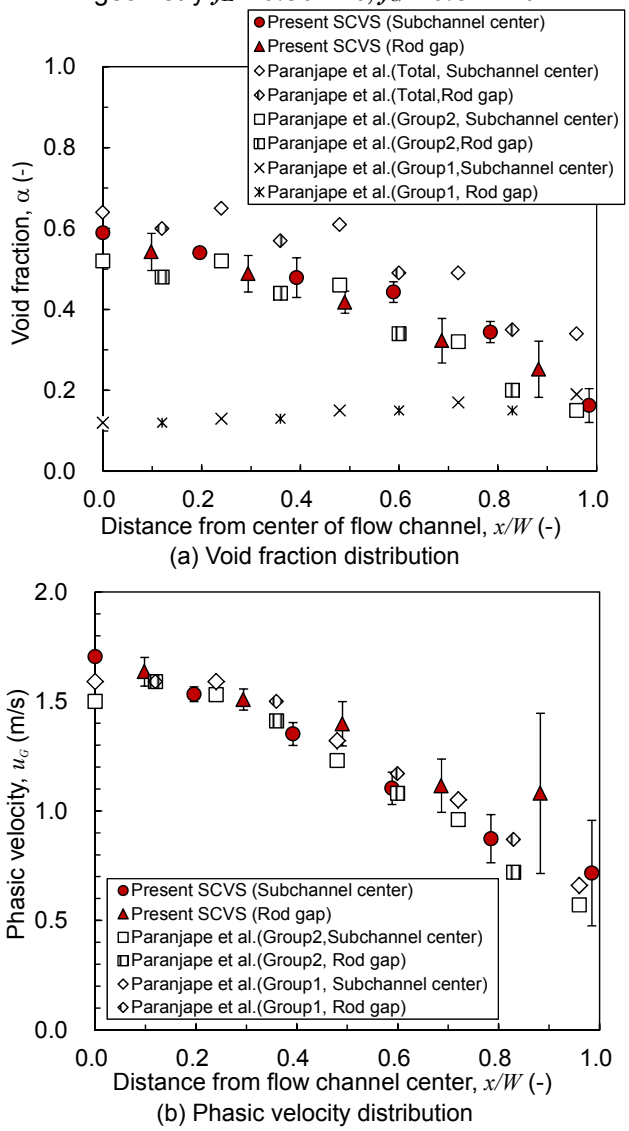

Fig.17 Comparison of results acquired with SCVS and conductance probe [6]

Kunihiko Nishiyama of Electric Power Engineering Systems Co., Ltd. for their assistance in these experiments.

REFERENCES

1. R. Maad, B.T. Hjertaker, *et al.*, Dynamic characterization of a high speed gamma-ray tomograph, *Flow Meas. Instrum*, Vol.21, No.4, pp.538-545, 2010.
2. T. Arai, M. Furuya, T. Kanai, Development of high-speed and multidimensional measurement technique for liquid film behavior, *Proc. 14th Int. Sym. Flow Visualization (ISFV14)*, pp.1-9, 2010.
3. H.-M. Prasser, et al., *Annual Report of Institute of Safety Research*, FZR-284, ISSN 1437-322X, 15, 2000.
4. H.-M. Prasser, A. Böttger, J. Zschau: A new electrode-mesh tomograph for gas-liquid flows, *Flow Meas. Instrum.*, Vol.9, No.2, pp.111 – 119, 1998.
5. T. Kanai, M. Furuya, K. Shirakawa, *et al*., Multi-dimensional Two-Phase Flow Measurements in a Large-Diameter Pipe Using Wire-Mesh Sensor, *Proc. 19th Int. Conf. Nucl. Engng.*, ICONE19-44020, 2011.
6. Paranjape, S. *et al.*: Modeling and measurement of interfacial area concentration in two-phase flow, *Nucl. Eng. Des.*, Vol. 240, No.9, pp.2329-2337, 2010.